Acta Pharmaceutica Sinica B 2019;9(1):167–176

Chinese Pharmaceutical Association
Institute of Materia Medica, Chinese Academy of Medical Sciences

Acta Pharmaceutica Sinica B

www.elsevier.com/locate/apsb
www.sciencedirect.com

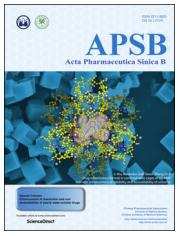

Efficient lung cancer-targeted drug delivery *via* a nanoparticle/MSC system

Xusheng Wang[a,†], Haiyan Chen[b,†], Xiaowei Zeng[a,†], Wenpeng Guo[c,†], Yu Jin[c,†], Shan Wang[d], Ruiyun Tian[d], Yanjiang Han[e], Ling Guo[f], Jimin Han[d], Yaojiong Wu[b,d,*], Lin Mei[a,*]

[a]*School of Pharmaceutical Sciences (Shenzhen), Sun Yat-sen University, Guangzhou 510275, China*
[b]*Tsinghua-Berkeley Shenzhen Institute (TBSI), Tsinghua University, Shenzhen 518055, China*
[c]*The First Affiliated Hospital of Shenzhen University (Shenzhen Second People's Hospital), Shenzhen 518000, China*
[d]*School of Life Sciences, Tsinghua University, Beijing 100084, China*
[e]*NanFang PET/CT Center, Nanfang Hospital, Southern Medical University, Guangzhou 510515, China*
[f]*Department of Biology and Shenzhen Key Laboratory of Cell Microenvironment, South University of Science and Technology of China, Shenzhen 518055, China*

Received 27 April 2018; received in revised form 26 June 2018; accepted 22 August 2018

KEY WORDS

Mesenchymal stem cells;
Nanoparticle;
Drug delivery;
Kras^{G12D};
Lung cancer

Abstract Low targeting efficiency limits the applications of nanoparticles in cancer therapy. The fact that mesenchymal stem cells (MSC) trapped in the lung after systemic infusion is a disadvantage for cell therapy purposes. Here, we utilized MSC as lung cancer-targeted drug delivery vehicles by loading nanoparticles (NP) with anti-cancer drug. MSC showed a higher drug intake capacity than fibroblasts. In addition, MSC showed predominant lung trapping in both rabbit and monkey. IR-780 dye, a fluorescent probe used to represent docetaxel (DTX) in NP, delivered *via* MSC accumulated in the lung. Both *in vitro* MSC/A549 cell experiments and *in vivo* MSC/lung cancer experiments validated the intercellular transportation of NP between MSC and cancer cells. *In vivo* assays showed that the MSC/NP/DTX drug delivery system exerted primary tumor inhibition efficiency similar to that of a NP/DTX drug system. Collectively, the MSC/NP drug delivery system is promising for lung-targeted drug delivery for the treatment of lung cancer and other lung-related diseases.

*Corresponding authors Tel./fax: +86 755 26036348.
E-mail addresses: wu.yaojiong@sz.tsinghua.edu.cn (Yaojiong Wu), meilin7@mail.sysu.edu.cn (Lin Mei).
†These authors made equal contributions to this work.

Peer review under responsibility of Institute of Materia Medica, Chinese Academy of Medical Sciences and Chinese Pharmaceutical Association.

https://doi.org/10.1016/j.apsb.2018.08.006

1. Introduction

Low targeting efficiency limits the applications of nanoparticles in cancer therapy[1–3]. Mesenchymal stem cells (MSC) have great potential for treating tissue injury and degenerative disease and for use in immune disorder therapy[4]. Additionally, anti-tumorigenic effects and low immunogenicity make MSC a kind of ideal vehicle for anti-tumor drug delivery[5,6]. While most MSC are trapped in the lung after intravenous administration, which is an unwanted result when MSC are used for cell therapy. Here, we utilized the disadvantage of MSC as an advantage in lung-targeted drug delivery. Even though drug-releasing MSC-mediated inhibition of lung metastasis has previously been described[7,8], more systemic studies are still desired. As a drug delivery vehicle, MSC showed larger NP/DTX intake capacities than fibroblasts. The *in vivo* distribution of MSC has been extensively studied in mice, but related studies have rarely been performed in larger animals, such as rabbits and monkeys[9,10].

About 30% of human tumors carry mutation of *RAS* gene[11–13]. Of the three genes in this family (composed of K-ras, N-ras and H-ras), K-ras is the most frequently mutated member in human tumors, including adenocarcinomas of the pancreas and lung[14,15]. $Kras^{G12D}$ mice were used in this study as *in vivo* tumor model to test tumor inhibit efficiency of the MSC drug delivery system. And MR imaging and Micro-PET-CT was performed to monitor tumor size and metabolism *in vivo*, respectively. In addition, intracellular processing of NP has been extensively explored, but intercellular transportation has rarely been studied. Here, we established 3D *in vitro* cell model to prove that NP could be intercellular transported from the MSC to A549 lung cancer cells, which was further supported by the *in vivo* lung cancer model.

There was study showed that mouse bone marrow MSC can be a reservoir for doxorubicin (DOX) and can be released not only in the form of DOX metabolites but also in its original and active form[16]. Further assay showed MSC efficiently absorb and release paclitaxel (PTX) in an active form. Similar result was observed in DOX and gemcitabine, and all these drug exhibit an inhibitory effect on tongue squamous cell carcinoma cells growth *in vitro*[17,18]. While it is still unclear that drug/NP in MSC could be released as an intact form or drug is released only after the NP was destroyed. This desire further evaluation and in this study both *in vitro* and *in vivo* models were used to circumvent these questions.

This study was designed to get further insight of the efficiency of drug uptake and tumor inhibiting efficiency of the drug/MSC system, and tried to interpret the underlying mechanism. First, this study verified the lung targeting ability of MSC in different animal model. Both *in vivo* and *in vitro* studies support the proposed intercellular transportation of NP from MSC to cancer cells. In addition, the MSC/NP/DTX system had tumor inhibition efficiency similar to that of NP/DTX but with only 1/8 the DTX dose. Thus, the MSC/NP drug delivery system is promising for lung-targeted drug delivery for the treatment of lung cancer. MSC may also be useful in lung-targeted drug delivery for chronic pneumonia treatment and other lung related diseases.

2. Materials and methods

2.1. Animals

The *Nu/Nu* mice (6–8 weeks old) used for cell and drug *in vivo* tracing were purchased from Guangdong Medical Laboratory Animal Center, Guangzhou, China. $Kras^{LSL\text{-}G12D}$ ($Kras^{G12D}$) mice (Jax® mice, Stock No: 008179) carrying a Lox-Stop-Lox (LSL) sequence followed by the K-ras G12D point mutation allele were used as a lung cancer model in this study. To induce lung cancer in $Kras^{G12D}$ mice, 7- to 8-week-old mice received 64 μL of cre-advenovirus (AdCre) solution through the nasal cavity. The virus solution was prepared by mixing 30 μL of AdCre (10^{10} pfu), 70 μL of EMEM, and 0.5 μL of 2 mol/L $CaCl_2$ and placed in room temperature for 20 min. Rabbits (3–4 months old, 3–4 kg, New Zealand white rabbits) were purchased from Guangdong Medical Laboratory Animal Center, Guangzhou, China. The monkey (*M. fascicularis*, 8 months old, 5 kg) used for *in vivo* tracing of NP and MSC was purchased from Pearl Laboratory Animal Sci. and Tech. Co. Ltd., Guangzhou, China. The animals were maintained in a temperature-controlled environment (20 ± 1 °C) with free access to food and water. All procedures were performed with the approval of the Animal Ethics Committee of Tsinghua University, Beijing, China.

2.2. MR imaging, micro-PET-CT and IVIS spectrum

For *in vivo* tracing of Fe_3O_4 NP and MSC in the monkey, 1 mL of iron oxide NP suspension (Aladdin Industrial Co., Ltd., Shanghai, China, 5 mg/mL) was mixed in MSC culture medium (1×10^7 MSC) for 5 h. The MSC were harvested and resuspended in 5 mL of PBS and injected into the monkey *via* the left arm vein. MR imaging of the monkey was performed at 1, 2, 3, 5, and 7 days post-MSC injection. MR imaging of the monkey before MSC injection was used as a blank control. For MR imaging of lung cancer in mice, MSC (1×10^6 cells carrying NP with ~25 μg of DTX) were resuspended in 100 μL of PBS and administered to AdCre-induced $Kras^{G12D}$ mice *via* intravenous injection. $Kras^{G12D}$ mice without AdCre induction and PBS-treated AdCre/$Kras^{G12D}$ mice served as negative controls, and AdCre/$Kras^{G12D}$ mice receiving DTX (10 mg/kg body weight) in NP were used as the positive control group. T2-weighted MR imaging of the monkey and mice were conducted with a 3 T MRI scanner, with slice thickness (SL) = 1.0 mm, repetition time (TR) = 5000 ms, and echo time (TE) from 10.6 to 159 ms.

A micro-PET/CT scan was performed on a SIEMENS Inveon scanner (Siemens Healthiness, Munich, Germany). The clinical package of ^{18}F-FDG (10 mCi) obtained from a regional vendor was diluted to 200 μCi/100 μL for each mouse/injection (200 μCi, 3.7 MBq). The FDG solution was drawn into a 1-mL syringe with a 26G 1/2-inch needle, and the radioactivity of the entire syringe was measured with a dose calibrator. The FDG solution was injected via an intravenous route, the injection time was recorded, and the residual radioactivity of the syringe was measured again with the dose calibrator. The animals were then incubated at room temperature for 1 h for FDG uptake. The injected FDG activity for each mouse was calculated using the following formula:

Injected activity (μCi) = activity in syringe before injection – activity in syringe after injection (1) Micro-PET/CT images were reconstructed using a 3D ordered subset expectation maximum (OSEM) algorithm, and CT correction was applied for attenuation correction. In the PET images, ROIs were measured with Inveon Research Workplace (IRW) 3.0 software (Siemens Healthiness, Munich, Germany). The ROI was determined by manually superimposing the ellipsoid volume of interest (VOI) to the target tissue. The activity concentrations were determined by the mean pixel intensity within each VOI and converted to μCi/mL using a

calibration constant. Assuming a tissue density of 1 g/mL, the ROI activity was converted to μCi/g and normalized as percent injected dose per gram (%ID/g).

Bioluminescence imaging of luciferase-labeled cell tracing in mice and rabbits and the fluorescence imaging of IR-780-labeled DTX were performed using an IVIS 100 camera (Caliper-PerkinElmer). For the cell tracing, IVIS imaging was performed 10 min after intraperitoneal injection of D-luciferin (10 mL/kg) at a concentration of 15 mg/mL in Dulbecco's PBS. For the IR-780-labeled DTX, the fluorescence imaging (excitation at 720 nm, emission at 780 nm) was performed at 3 and 12 h after the drug injection.

2.3. Cell culture, 3D cell spheres and cell imaging

Human MSC were isolated from human placenta and cultured as described previously. A549 cells were purchased from the American Type Culture Collection (ATCC, Rockville, MD, USA) and cultured in DMEM (Gibco-Invitrogen) supplemented with 10% (*v/v*) FBS (Gibco-Invitrogen) and 1% (*v/v*) antibiotics (100 units/mL penicillin and 100 μg/mL streptomycin). MSC and A549 cells were seeded on 100-mm culture dishes, and when cells reached 40% confluence, the medium was exchanged with 5 mL of new medium containing 40 μL of 1.0×10^{10} pfu GFP-adenovirus or Ad-tdTomato-adenovirus or luciferase-adenovirus for 24 h to obtain GFP-MSC, tdTomato-A549 cells, and luciferase-MSC, respectively. Human mammary fibroblasts (HMFs) were cultured in DMEM supplemented with 10% calf serum (CS), 2 mmol/L L-glutamine, and penicillin/streptomycin. All cultures were maintained at 37 °C in a humidified atmosphere containing 5% CO_2.

To form 3D spheroids, passage 5–7 MSC and A549 cells were cultured using a hanging drop method. Briefly, GFP-MSC and tdTomato-A549 cells were mixed at a ratio of 1:2, with a total of 30,000 cells in 35 μL of growth medium per drop were plated in hanging drops and incubated for 36 h to form spheroids. Then, the spheroids were collected to obtain frozen tissue sections and for microscopic analysis.

MSC grown on coverslips were fixed in 1% PFA (paraformaldehyde). MSC and A549 cell spheroids were fixed in 3% PFA and embedded in OCT for tissue sectioning (8–10 μm thickness). Nuclei were stained with 4,6-diamidino-2-phenylindole (DAPI). After mounting, samples were visualized under a confocal microscope (FV1000; Olympus, Tokyo, Japan). The 3D cell imaging was performed under an Olympus FluoView FV1000 two-photon microscope with an Olympus 25 × 1.0 NA water-immersion objective lens. A Spectra Physics Mai-Tai IR laser was tuned to 920 nm for two-photon excitation of GFP and tdTomato.

2.4. Nanoparticle/DTX formation, MSC intake and LC–MS assay

Poly(lactide-*co*-glycolide) (PLGA, MW = 10,000), D-α-tocopheryl polyethylene glycol 1000 succinate (TPGS), *N*-hydroxysuccinimide (NHS), 1,3-diisopropylcarbodiimide (DCC), triethylamine (TEA) and IR-780 were purchased from Sigma–Aldrich (St. Louis, MO, USA). Docetaxelwas provided by Shanghai Jinhe Bio-Technology Co., Ltd. (Shanghai, China). Doxorubicin hydrochloride (DOX-HCl) was purchased from Dalian Meilun Biology Technology Co., Ltd. (Dalian, China). Methoxy-poly(ethylene glycol)-amine (M-PEG-NH_2, MW = 2000) and FITC-poly(ethylene glycol)-amine (FITC-PEG-NH_2, MW = 2000) were purchased from Shanghai Yare Biotech, Inc. (Shanghai, China). Cy5-poly (ethylene glycol)-amine (Cy5-PEG-NH_2, MW = 2000) was provided by Xi'an ruixi Biological Technology Co., Ltd. (Xi'an, China). All other chemicals and reagents were of the highest quality and were commercially available and used as received.

The copolymer PLGA-*b*-PEG was synthesized as described in our previous report. In brief, PLGA (5.0 g, 0.5 mmol) dissolved in anhydrous dichloromethane was activated by DCC (0.206 g, 1 mmol) and NHS (0.115 g, 1 mmol) at room temperature for 24 h under dry argon. The reaction byproduct dicyclohexylcarbodiurea (DCU) was removed by filtration, and the activated PLGA (PLGA-NHS) was precipitated in anhydrous ether, filtered and washed with methanol. The PLGA-NHS was dried in vacuo at 40 °C for 24 h. The PLGA-NHS (2 g, 0.2 mmol) was dissolved in 25 mL of anhydrous dichloromethane. Then, M-PEG-NH_2 (0.5 g, 0.25 mmol) was added to the organic solution under magnetic stirring. The reaction was carried out for 12 h under a dry argon atmosphere, and the resulting solution was precipitated in cold anhydrous ether. The precipitated copolymer PLGA-*b*-PEG was filtered, washed with methanol, and finally dried under vacuum for 24 h. Moreover, the fluorescence-labeled copolymers PLGA-*b*-PEG-FITC and PLGA-*b*-PEG-Cy5 were prepared using the same procedure except FITC-PEG-NH_2 and Cy5-PEG-NH_2, respectively, were used in the reaction instead of M-PEG-NH_2. A routine assay for nanoparticle size was performed, the nanoparticle size was ranged from 50–200 nm.

The anti-cancer drug DTX-loaded PLGA-*b*-PEG NP were prepared using a modified nanoprecipitation method as previously described. Briefly, 10 mg of DTX powder and 100 mg of the copolymer PLGA-*b*-PEG were dissolved in 8 mL of acetone by vortexing. This solution was added dropwise to 100 mL of aqueous solution containing 0.03% TPGS under stirring. The mixture was then stirred uncovered overnight to completely remove the acetone. The NP suspension was centrifuged at 20,000 rpm (Backman, J-30I, CA, USA) for 15 min and then washed three times to remove the emulsifier TPGS and unencapsulated drug. Finally, the resulting product, DTX-loaded PLGA-*b*-PEG NP (designated as NP/DTX), was obtained by lyophilization. IR-780-loaded PLGA-*b*-PEG NP (designated as NP/IR-780) and fluorescent dye Cy5-labeled drug-free PLGA-*b*-PEG-Cy5 NP (designated as Cy5-NP) were prepared in a similar manner. For preparation of DOX-loaded PLGA-*b*-PEG-FITC NP (designated as FITC-NP/DOX), 10 mg of DOX-HCl was neutralized with an excess amount of TEA and 100 mg of the copolymer PLGA-*b*-PEG-FITC were dissolved in 8 ml of acetone. Then, the solution was added dropwise into 100 ml of aqueous solution containing 0.03% TPGS under stirring in the dark. The subsequent procedure was similar to that of the formulation of NP/DTX. The size and size distribution of NP were measured using dynamic light scattering (DLS) with a Malvern Mastersizer 2000 (Zetasizer Nano ZS90, Malvern Instruments Ltd., UK). The morphology of the NP was observed with transmission electron microscopy (TEM, Tecnai G2 20, FEI Company, Hillsboro, Oregon, USA). The prepared NP were approximately 120–130 nm in diameter, which potentially resulted in high cellular uptake through endocytosis. The size distribution and TEM images of NP/DTX are

shown in Supporting Information Fig. S1. The NP were nearly spherical and approximately 100 nm in size (smaller than the size obtained using a DLS analysis). This difference can be ascribed to the tendency of NP to shrink and collapse when dried.

GFP-MSC and MSC were plated at a density of 4.0×10^5 cells per 100-mm well in glass-bottomed dishes (MatTek Corporation), when cells reached 80% confluence, the medium was exchanged with 5 mL of new medium containing 100 μL of 2 mg/mL Nano/DTX. After 3 h, the cells were collected and resuspended in PBS, and 1.0×10^6 MSC in 100 μL of PBS were injected into mice *via* the tail vein.

LC/MS analysis was performed on a system equipped with an Alliance HPLC Waters 2695 system (Waters, USA) and a Quattro Premier XE mass spectrometer (Waters, USA). The MS system consisted of an ESI interface and a triple quadrupole (QqQ) mass analyzer. The MS parameters were as follows. Capillary voltage was set at 3.0 kV in positive ion mode. Source temperature was maintained at 130 °C, while the desolvation temperature was set at 300 °C. N_2 was used as the desolvation gas (flow rate of 800 L/h) and cone gas (flow rate of 60 L/h), and Ar was used as the collision gas (flow rate of 0.15 mL/min). The MS and MS/MS spectra were obtained in MS scan mode and daughter scan mode, respectively. The quantification was performed in multi-reaction monitoring (MRM) mode.

2.5. *Western blotting*

Cell lysates were prepared in a lysis buffer containing 1% Triton X-100, 1% deoxycholic acid, 2 mmol/L $CaCl_2$ and protease inhibitors (10 μg/mL leupeptin, 10 μg/mL aprotinin, 1.8 mg/mL iodoacetamide and 1 mmol/L phenylmethyl sulfonyl fluoride) and quantified with a BCA protein assay kit (Pierce). Equal amounts of total protein were subjected to electrophoresis on 12% bis-Tris gels, transblotted onto nitrocellulose membranes and probed with the primary antibody anti-clathrin [D3C6] (1:500, Cell Signal Technology, No. 4796) followed by peroxidase-conjugated secondary antibody (GeneTex). Immunoreactive bands were detected using an ECL kit according to the manufacturer's instructions. Subsequent reprobing using anti-glyceraldehyde-3-phosphate dehydrogenase (GAPDH) was performed as an internal loading control.

2.6. *Statistical analyses*

Results are expressed as the mean ± SEM unless stated otherwise. Statistical comparisons between two groups were evaluated with Student's *t*-test (unpaired *t*-test, two-tailed). A probability (*P*) value of 0.05 was considered to indicate statistical significance.

3. Results

3.1. *MSC have great capacity in nanoparticle/drug intake*

First, to explore the drug intake capacity of MSC, immunofluorescence (IF) staining was utilized, and extensive NP (PLGA-PEG-FITC, the NP was 50–200 nm in diameter and the electron microscope image was showed in Fig. 1a) and doxorubicin (DOX) aggregation was detected 3 h after DOX/NP intake (Fig. 1b). An LC–MS quantitative assay of the DTX dose at 1, 3, 7, 12, and 24 h after MSC intake showed that DTX intake reached a peak at 12 h, with over 36 μg in 10^6 MSC, compared to only 15 μg of DTX detected in the same number of fibroblasts (Fig. 1c), indicating the high capacity of MSC for NP/DTX intake. This result was further supported by the significantly increased expression of clathrin, an important mediator of endocytosis, in

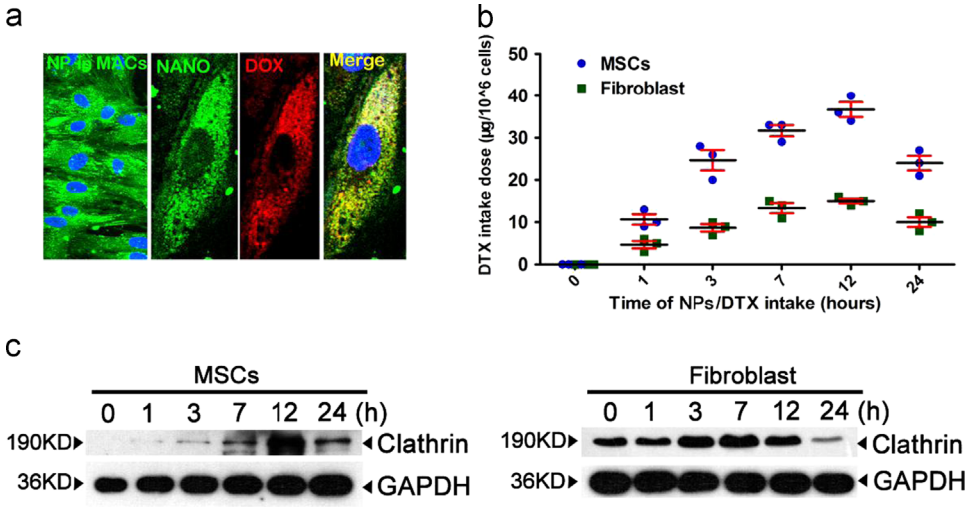

Figure 1 Drug intake capacity of MSC and *in vivo* distribution of drug, NP and MSC. (a)The size assay of PLGA-PEG nanoparticles. Upper, the size distribution of nanoparticle. Lower, the electron microscopy image of the nanoparticle. Scale bar: 200 nm. (b) An abundance of nanoparticles (green, left) and doxorubicin (DOX, red)-loaded nanoparticles (green) were taken up by MSC (right). NP, nanoparticles. A representative result from more than 5 independent experiments is shown. Scale bar, 10 μm. (c) Quantitative analysis of DTX intake by MSC and fibroblasts. DTX intake by MSC peaked at 12 h with 30 μg of DTX in 10^6 cells. Comparatively, the DTX intake by fibroblasts peaked at 12 h with 15 μg of DTX in 10^6 cells. $n = 3$ for both MSC and fibroblasts at each time point. (d) Western blotting analysis of clathrin expression at 1, 3, 7, 12, and 24 h after NP intake by both MSC and fibroblasts. Four independent experiments were performed.

MSC (Fig. 1d). These data support that MSC have a great potential in nanoparticle/drug intake.

3.2. *MSC are lung-predominant distributed in mice, rabbits and monkey*

The lung-predominant distribution of MSC in mice was further confirmed with an *in vivo* imaging system (IVIS) assay, which showed that luciferase-labeled MSC (Luci-MSC) were only detected in the lung 24 h after injection (upper); *ex vivo* imaging showed similar results (lower) (Fig. 2a). Furthermore, 3D reconstruction imaging of the *in vivo* distribution of MSC in mice indicated that Luci-MSC uniquely merged in lung position (Fig. 2b). Intravenous injection of Luci-MSC in rabbits revealed that the luciferase signal could only be detected in the lung 12 h after injection, and *ex vivo* imaging showed a uniform distribution in lung tissue (Fig. 2c). In this study, a *cynomolgus monkey* was used to further analyze the *in vivo* distribution of NP and MSC in primates. To detect MSC in monkey, MSC infused with iron oxide (Fe_3O_4) NP were intravenously injected into the monkey, Magnetic resonance imaging (MRI) showed that Fe_3O_4 NP signal is extensively detected in the lung on the 1st day after injection, and the MSC in the monkey lung tissue were maintained for approximately 5 days (Fig. 2d). These result proved that MSC are lung-predominant distributed in both small and large animals.

3.3. *The duration of MSC and the target of MSC/NP system in vivo*

Low immunogenicity is a significant feature of allogenic transplantation of MSC. In this study, a comparative assay was performed to study the *in vivo* duration of MSC. MSC, fibroblast and RAW264.7 cells were equally transfected with Lenti-Luciferase virus, and infused to mice *via* intravenous injection. The *in vivo* distribution and tracing

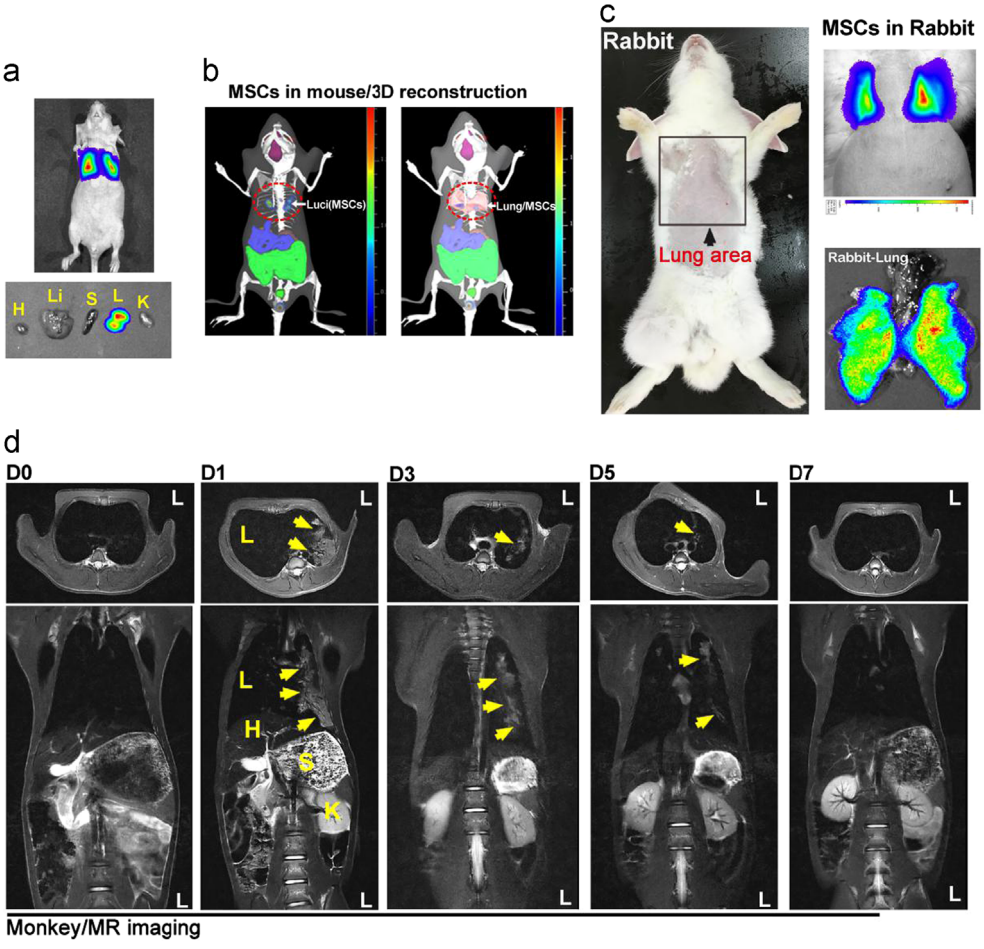

Figure 2 *In vivo* tracing of MSC in mice, rabbits and monkey. (a) *In vivo* imaging system (IVIS) assays showed that MSC (luciferase expression, bioluminescence signal) could only be detected in the lung area of mice. *Ex vivo* analysis of different mouse organs showed similar results. $n = 10$ mice, 3 rabbits. H, heart; Li, liver; S, spleen; L, lung; K, kidney. (b) 3D reconstruction imaging of the *in vivo* distribution of MSC in mice. Results are representative of more than 3 independent experiments. (c) IVIS assay of MSC in rabbit, a strong bioluminescence signal was detected in both *in vivo* and *ex vivo* assay of rabbit lung. $n = 3$ rabbits. The results shown were obtained from 3 independent experiments. (d) MR imaging assay of iron oxide (Fe_3O_4) nanoparticle-labeled MSC in a cynomolgus monkey, MRI assays were performed at 0 (before MSC/NP injection), 1, 3, 5, and 7 days post-injection of MSC/NP. $n = 1$ monkey, and 1 MRI assay was performed at each time point. L, lung; H, heart; S, stomach; K, kidney.

of these cells were assayed by IVIS at 1, 3, 5 and 7 days after cell injection. The result showed that MSC were only detected in the lung area and maintained at least for 7 days, while the fibroblasts and RAW264.7 cells were detected in other tissues and maintained only for approximately 3 days (Fig. 3a). To analyze the *in vivo* drug distribution of the MSC/NP drug delivery system, IR780 was used for *in vivo* drug tracing. Briefly, 1×10^6 MSC carrying NP/IR780 were injected into nude mice, and an IVIS imaging spectrum was obtained 3 and 12 h after injection; regular NP/IR780 were injected as the control group. The results showed that at 3 h after injection the IR780 signal in the lung area in the MSC/NP/IR780 system composed ~60% of the whole body signal, and the ratio was 25% for the NP/IR780 injection. At 12 h, the IR780 signal ratios in the lung area in the MSC/NP/IR780 and NP/IR780 groups were approximately 80% and 20%, respectively (Fig. 3c and d), this result was further supported by *ex vivo* data of MSC/NP/IR780 distribution in different organ (Fig. 3e). In conclusion, MSC are long-time maintained *in vivo*, and MSC/NP system could efficiently target the drug to lung tissue.

3.4. *Nanoparticles were intercellular transported from MSC to cancer cells in both vitro and in vivo model*

There are two possible approaches for the transport of the anti-cancer drug in the MSC/NP system to the lung cancer cells; one approach is the release of the drug from the MSC followed by drug intake by the lung cancer cells, and the other approach is the release of a NP/drug package by MSC followed by the uptake of the NP/drug package by the lung cancer cells. To verify that NP can be transported intercellularly between MSC and lung cancer cells, both *in vivo* and *in vitro* studies were performed. For the *in vitro* study, MSC (GFP-labeled) and A549 (lung cancer cell line, tdTomato-labeled) cells were co-cultured in hanging drop medium to form 3D spheres (Fig. 4a) in which Cy-5-labeled PLGA-PEG NP were carried in MSC. Imaging of 3D sphere sections showed that 36 h after co-culture, the NP diffused dynamically from MSC to A549 cells (Fig. 4b). For the *in vivo* analysis, GFP-labeled and Cy5-NP-carrying MSC were

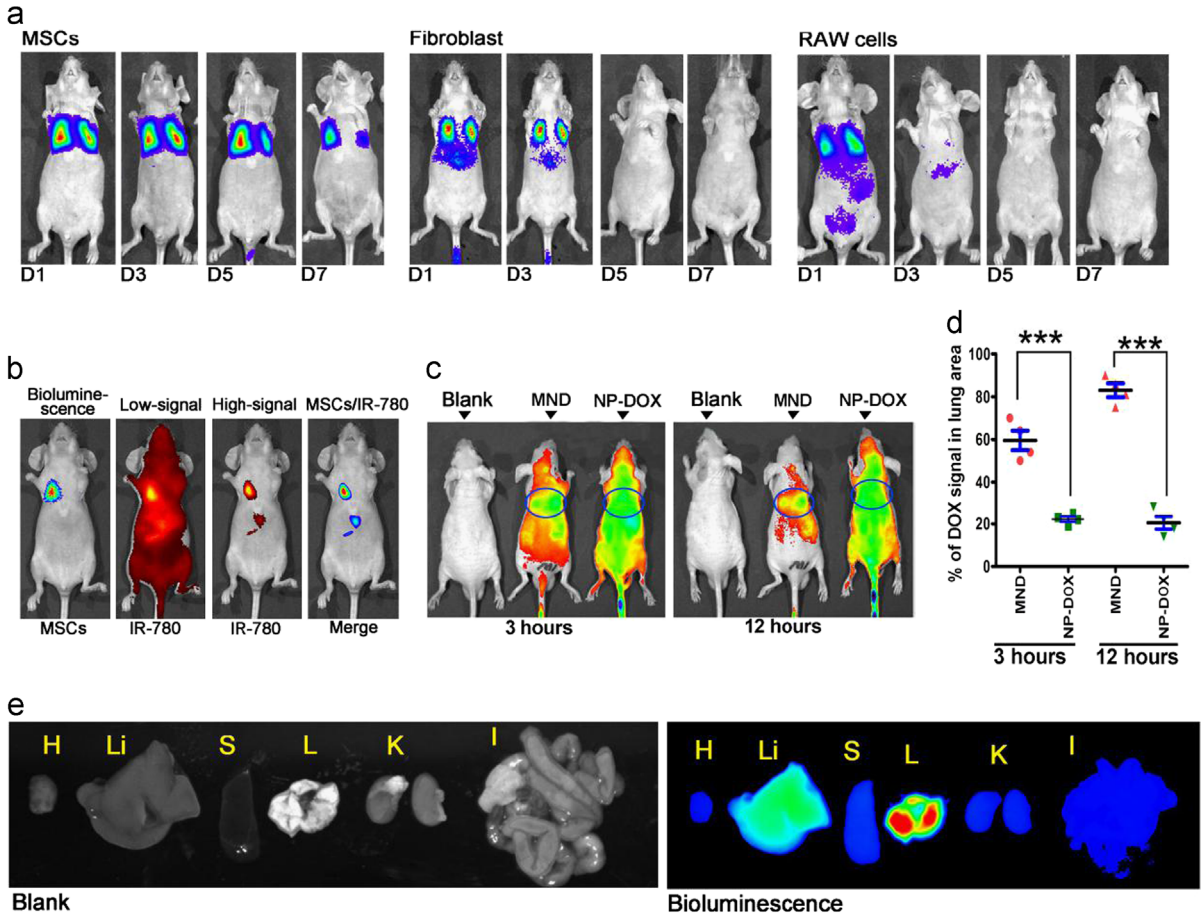

Figure 3 Lung-target efficiency of drug loaded MSC/NP system. (a) MSC, fibroblasts and RAW264.7 cells were labeled with luciferase, and the *in vivo* distribution and tracing of these cells was assayed using IVIS, which was performed at 1, 3, 5 and 7 days after cell injection. MSC were only detected in the lung area and were maintained for at least for 7 days, while the fibroblasts and RAW264.7 cells were detected in other tissues and maintained for approximately 3 days. $n = 5$–8 mice for each group. (b) *In vivo* tracing and co-localization of MSC and IR-780 in the MSC/NP system. A representative result from more than 3 independent experiments is shown. (c) and (d) *In vivo* monitoring of IR-780 distribution in mice at 3 and 12 h post i.v. injection (c), and quantitative assay of the ratio of IR-780 signaling in the lung area of mice from different groups at two time points (d). (e) *Ex vivo* result of MSC/NP/IR780 distribution in different organ 6 h after MSC infusion. H, heart; Li, liver; S, spleen; L, lung; K, kidney; I, intestine. The results are representative of 5 independent experiments. The data are expressed as the mean ± SEM $^{***}P < 0.001$, unpaired *t*-test, two-tailed. NP, Nanoparticles; MND, MSC/NP/DOX; DOX, Doxorubicin.

intravenously injected into Cre-virus induced *Kras*^{G12D} mice with primary lung cancer. Lung tissue sections revealed that there was also extensive diffusion of NP from MSC to adjacent lung cells (Fig. 4c). These *in vivo* and *in vitro* results indicate that dynamic intercellular NP transportation occurred between MSC and cancer cells.

3.5. *MSC/NP/DTX system efficiently inhibit tumor growth in vivo*

To assay the *in vivo* tumor inhibition efficiency of the MSC/NP/DTX system, a lung cancer and tumor inhibit model in *Kras*^{G12D} mice was established (Fig. 5a). In the MSC/NP/DTX group, 1×10^6 MSC with NP/DTX (MSC) was injected intravenously every 5 days. The NP/DTX group (DTX dose, 10 mg/kg body weight) was also injected at an equal dose into a control group. Thirty days after tumor initiation, a PET-CT assay showed that there was significantly higher ^{18}F-FDG uptake in the lungs of the lung cancer model group. Consistently, an MRI assay showed that there was obvious tumor formation. Comparatively, the PET-CT assay did not show notably higher uptake of ^{18}F-FDG in the lungs of the NP/DTX-treated group, and the MRI results showed that there was a small amount of tumor formation. Importantly, in the MSC/NP/DTX-treated group, the PET-CT and MRI showed results similar to those of the NP/DTX group, with

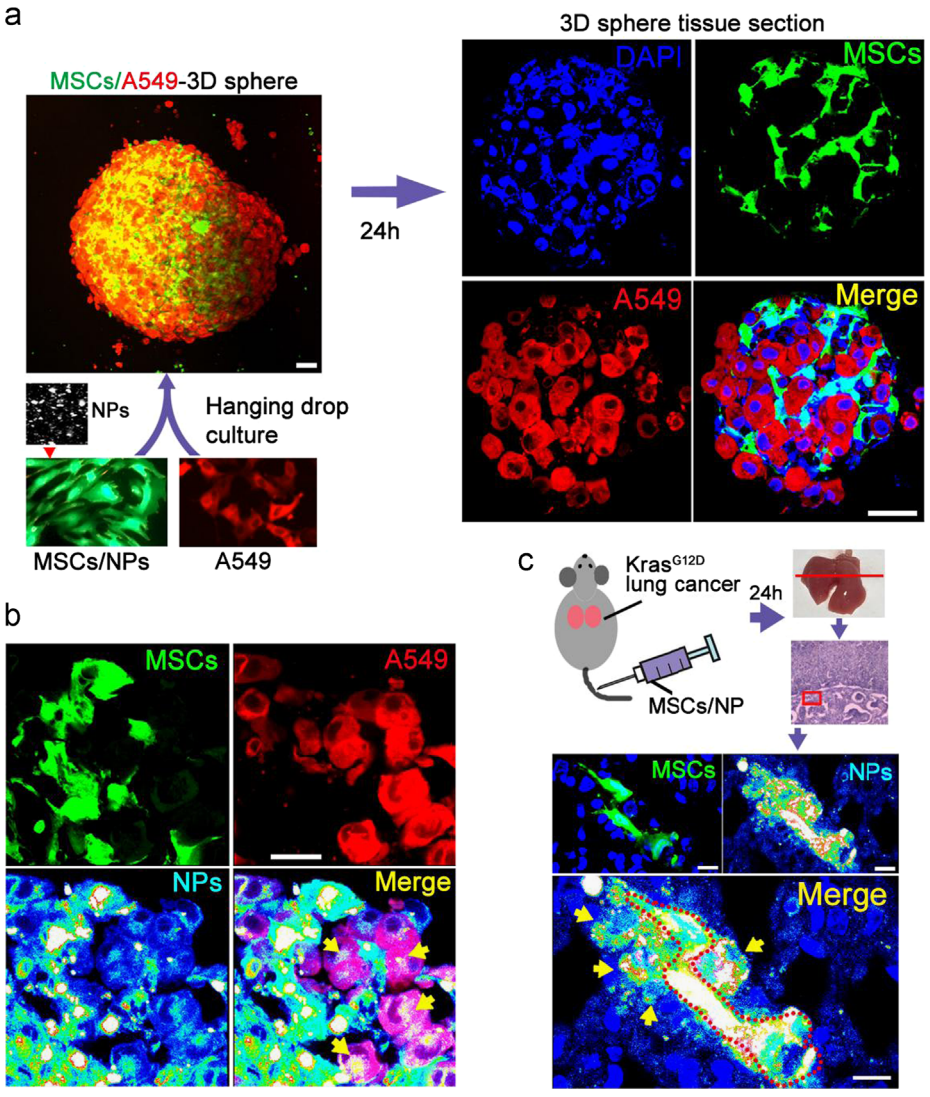

Figure 4 Intercellular transportation of NP in the MSC/NP system. (a) GFP-labeled MSC (carrying Cy5 nanoparticles) and tdTomato-labeled A549 cells formed 3D spheres after incubation in a hanging drop culture. Scale bar, 30 μm. For tissue section assays, a representative result is shown from over 6 sections of 4–6 spheres or tissues. (b) In tissue section assays, numerous Cy5-nanoparticles were detected in A549 cells, indicating dynamic intercellular transportation of nanoparticles between MSC and cancer cells. Scale bar, 20 μm. (c) GFP-labeled and Cy5-nanoparticle-carrying MSC were infused into *Kras*^{G12D} lung cancer tumor mice *via* i.v. injection. Tissue section imaging was performed 24 h later, and Cy5-nanoparticles were detected in lung cells adjacent to the MSC. Scale bar, 20 μm.

lower ^{18}F-FDG uptake and less tumor formation than the lung cancer model group (Fig. 5b). In addition, tumor weights on the 35th day after primary tumor initiation further confirmed that MSC/NP/DTX and NP/DTX treatment exhibited similar tumor inhibition efficiency (Fig. 5c). The *ex vivo* assay of the lung tissues (21st day post-Add-Cre induction) from mice in the 4 different groups further validated the tumor inhibition capacity of the MSC/NP/DTX system. The ^{18}F-FDG intake in the MSC/NP/DTX group was greatly reduced and was quantified as the percent injected dose per gram of tissue (%ID/g) with a decay correction ($P<0.001$) (Fig. 5d and e). Accordingly, the lung volume in the MSC/NP/DTX group was significantly less than that in the lung cancer group ($P<0.001$, Fig. 5f). These data indicate efficient *in vivo* lung tumor inhibition of the MSC/NP/DTX system.

4. Discussion

The promising features of MSC, including their regenerative potential and capacity to differentiate into different cell lineages, have generated great interest of scientists to engage in more studies with intriguing perspectives on cell-based therapies[19–21]. MSC are the most commonly used adult stem cells in regenerative medicine that can be isolated from several tissues, exhibit a strong capacity for replication *in vitro*, and can differentiate into osteoblasts, chondrocytes, and adipocytes[22–24]. Currently, hundreds of MSC-based clinical trials, either complete or ongoing, appear in the database of the US National Institutes of Health[25–27].

In this study, we tried to utilize MSC as a drug carrier to deliver DTX to lung tumors. There are three obvious advantage for MSC used as lung-targeted drug carrier. Firstly, MSC can be easily

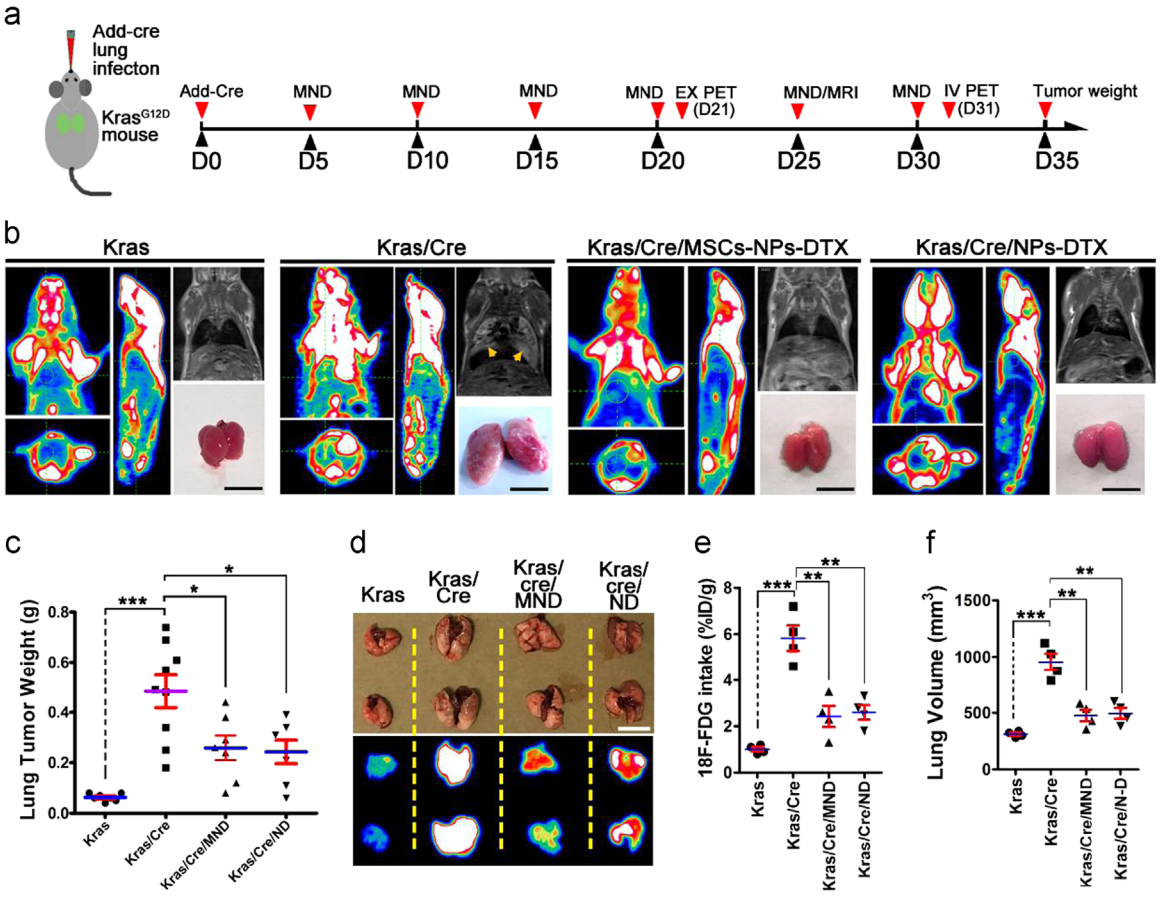

Figure 5 Tumor inhibition efficiency of the MSC/NP/DTX system. (a) Schematic of *in vivo* tumor inhibition assay using MSC/NP/DTX in *Kras*^{G12D} mice. (b) The tumor inhibition efficiency of the MSC/NP/DTX system was determined in Cre-induced lung cancer in *Kras*^{G12D} mice. Equal administration of NP/DTX served as a drug control, and non-induced *Kras*^{G12D} mice served as a negative control. MRI was performed on the 25th day after tumor induction to evaluate tumor formation in different groups. PET-CT was performed to evaluate the ^{18}F-FDG uptake on the 35th day, and tumor size was determined on the 40th day. Representative results from 6–8 mice are shown for each assay. Scale bar, 1 mm. (c) Quantitative assay of the tumor weights of different groups was performed on the 40th day after tumor induction; $n=6$–10 mice per group. (d) ^{18}F-FDG uptake in an *ex vivo* PET-CT assay of tumors from mice in four different groups on the 30th day after induction. (d) and (e) A quantitative assay to assess tumor volume (d) and the mean ID of ^{18}F-FDG (e) was performed; $n=4$ mice per group. MND, MSC/NP/DTX; ND, NP/DTX. Scale bar, 1 mm. The data are expressed as the mean ± SEM $^{*}P<0.05$, $^{**}P<0.01$, and $^{***}P<0.001$, unpaired *t*-test, two-tailed.

isolated and cultured from bone marrow of the patients[28], and transplanted into patients again for treatment to avoid immune rejection[29]. Secondly, it is now well-accepted that MSC exhibit a natural high tumor affinity, which allows them to home to tumors and then retain in tumors *in vivo* although the detailed mechanism remains unclear[30,31]. Above all, lung-predominant distribution is the most significant feature of MSC used as lung-targeted drug carrier. In this study, MSC are majorly distributed in lung after intravenous injection in mice, rabbits and monkey. While all the transplanted MSC are xenogenic, thus a systematical study of the *in vivo* maintenance and tumor inhibit efficiency of an allogenic or autogenic MSC are still desired. The intercellular transportation of nanoparticle between MSC and cancer cells was proved in this study, while the underlying mechanism still need further exploration. Probably, the nanoparticle intercellular transportation was proceeded an exocytosis-endocytosis procedure. In addition, the intercellular transportation efficiency need to be determined with an elegant method.

Exosomes also have been exploited as drug delivery vehicles for anti-cancer drugs in several studies, in which exosomes or exosome-like vesicles loaded with Dox or PTX. The chemotherapeutics were shown to traffic to tumor tissues and reduce tumor growth in mice and without the effects that observed mice that treated with free drug[32,33]. Pascucci et al.[17] observed that PTX-treated MSC mediated anti-tumorigenic effects because of their capacity to uptake the drug and subsequently release it in extracellular vesicles. Further assay showed that exosome vesicles fused more effectively with the cancer cell membrane than polymer-based synthetic nanoparticles. Intriguingly, even we observed the intercellular transportation of nanoparticles between MSC and their nearby A549 cells, it still unclear whether this process was mediated by exosomes released by MSC. And it will be interesting to explore the role of exosomes in the intercellular transportation of nanoparticle between different cells.

Collectively, this study quantified the DTX intake capacity of MSC and verified the lung targeting ability of MSC, NP and a drug mimic in an MSC/NP drug delivery system. Both *in vivo* and *in vitro* studies support the proposed intercellular transportation of NP from MSC to cancer cells. In addition, the MSC/NP/DTX system had tumor inhibition efficiency similar to that of NP/DTX but with only 1/8 the DTX dose. Given the passive lung targeting ability, low immunogenicity and tissue repair-promoting of MSC and the extensive pre-clinical and clinical research basis for application of MSC, MSC may also be useful in lung-targeted drug delivery for chronic pneumonia treatment and other lung related diseases, in addition to being used as a drug carrier for primary and metastatic lung cancer treatment.

Acknowledgments

We thank Changjun Tian for assistant with MR imaging assay, Tianbin Wang for PET-CT assay and Qince Sun for IVIS assay. This work was supported by grants from the Natural Science Foundation of China (Nos. 81771966, 31371404, 31401187 and 31571429), the Fundamental Research Funds for the Central Universities (Lin Mei, China), the Guangdong Natural Science Funds for Distinguished Young Scholar (No. 2014A030306036, China), the Natural Science Foundation of Guangdong, China (2015A030311041, 2015A030313763), Science and Technology Planning Project of Guangdong Province, China (Nos. 2016A020217001 and 2014A020212466), the Shenzhen Science and Technology Innovation Committee (JCYJ20160301152300347, JCYJ20160531195129079, JCYJ20170412095722235, JCYJ2016042-9171931438, and GJHZ20150316160614842, China) and Guangdong Province Medical Science and Technology Research Fund (A2016445, China).

Appendix A. Supporting information

Supplementary data associated with this article can be found in the online version at http://dx.doi.org/10.1016/j.apsb.2018.08.006.

References

1. Cheng W, Nie JP, Gao NS, Liu G, Tao W, Xiao XJ, et al. A multifunctional nanoplatform against multidrug resistant cancer: merging the best of targeted chemo/gene/photothermal therapy. *Adv Funct Mater* 2017;**27**:1704135.
2. Zhang M, Kim YK, Cui PF, Zhang JL, Qiao JB, He YJ, et al. Folate-conjugated polyspermine for lung cancer-targeted gene therapy. *Acta Pharm Sin B* 2016;**6**:336–43.
3. Huang ZX, Xie Q, Guo QP, Wang KM, Meng XX, Yuan BY, et al. DNA aptamer selected for specific recognition of prostate cancer cells and clinical tissues. *Chin Chem Lett* 2017;**28**:1252–7.
4. Islam MN, Das SR, Emin MT, Wei M, Sun L, Westphalen K, et al. Mitochondrial transfer from bone-marrow-derived stromal cells to pulmonary alveoli protects against acute lung injury. *Nat Med* 2012;**18**:759–65.
5. Qiao L, Xu Z, Zhao T, Zhao Z, Shi M, Zhao RC, et al. Suppression of tumorigenesis by human mesenchymal stem cells in a hepatoma model. *Cell Res* 2008;**18**:500–7.
6. Lee M, Jeong SY, Ha J, Kim M, Jin HJ, Kwon SJ, et al. Low immunogenicity of allogeneic human umbilical cord blood-derived mesenchymal stem cells *in vitro* and *in vivo*. *Biochem Biophys Res Commun* 2014;**446**:983–9.
7. Pessina A, Leonetti C, Artuso S, Benetti A, Dessy E, Pascucci L, et al. Drug-releasing mesenchymal cells strongly suppress B16 lung metastasis in a syngeneic murine model. *J Exp Clin Cancer Res* 2015;**34**:82.
8. Zhao Y, Tang S, Guo J, Alahdal M, Cao S, Yang Z, et al. Targeted delivery of doxorubicin by nano-loaded mesenchymal stem cells for lung melanoma metastases therapy. *Sci Rep* 2017;**7**:44758.
9. Gao J, Dennis JE, Muzic RF, Lundberg M, Caplan AI. The dynamic *in vivo* distribution of bone marrow-derived mesenchymal stem cells after infusion. *Cells Tissues Organs* 2001;**169**:12–20.
10. Barbash IM, Chouraqui P, Baron J, Feinberg MS, Etzion S, Tessone A, et al. Systemic delivery of bone marrow-derived mesenchymal stem cells to the infarcted myocardium: feasibility, cell migration, and body distribution. *Circulation* 2003;**108**:863–8.
11. Bos JL. Ras oncogenes in human cancer—a review. *Cancer Res* 1989;**49**:4682–9.
12. Avruch J, Zhang XF, Kyriakis JM. Raf meets Ras—completing the framework of a signal-transduction pathway. *Trends Biochem Sci* 1994;**19**:279–83.
13. Khosravifar R, Der CJ. The Ras signal transduction pathway. *Cancer Metastas- Rev* 1994;**13**:67–89.
14. Mills NE, Fishman CL, Rom WN, Dubin N, Jacobson DR. Increased prevalence of K-*Ras* oncogene mutations in lung adenocarcinoma. *Cancer Res* 1995;**55**:1444–7.
15. Pellegata NS, Sessa F, Renault B, Bonato M, Leone BE, Solcia E, et al. K-*Ras* and p53 gene-mutations in pancreatic-cancer—ductal and nonductal tumors progress through different genetic lesions. *Cancer Res* 1994;**54**:1556–60.
16. Pessina A, Piccirillo M, Mineo E, Catalani P, Gribaldo L, Marafante E, et al. Role of SR-4987 stromal cells in the modulation of doxorubicin toxicity to *in vitro* granulocyte-macrophage progenitors (CFU-GM). *Life Sci* 1999;**65**:513–23.

17. Pascucci L, Cocce V, Bonomi A, Ami D, Ceccarelli P, Ciusani E, et al. Paclitaxel is incorporated by mesenchymal stromal cells and released in exosomes that inhibit *in vitro* tumor growth: a new approach for drug delivery. *J Control Release* 2014;**192**:262–70.
18. Cocce V, Farronato D, Brini AT, Masia C, Gianni AB, Piovani G, et al. Drug loaded gingival mesenchymal stromal cells (GinPa-MSCs) inhibit *in vitro* proliferation of oral squamous cell carcinoma. *Sci Rep* 2017;**7**:9376.
19. Le Blanc K, Rasmusson I, Sundberg B, Gotherstrom C, Hassan M, Uzunel M, et al. Treatment of severe acute graft-versus-host disease with third party haploidentical mesenchymal stem cells. *Lancet* 2004;**363**:1439–41.
20. Horwitz EM, Prockop DJ, Fitzpatrick LA, Koo WW, Gordon PL, Neel M, et al. Transplantability and therapeutic effects of bone marrow-derived mesenchymal cells in children with osteogenesis imperfecta. *Nat Med* 1999;**5**:309–13.
21. Shi YF, Hu GZ, Su JJ, Li WZ, Chen Q, Shou PS, et al. Mesenchymal stem cells: a new strategy for immunosuppression and tissue repair. *Cell Res* 2010;**20**:510–8.
22. Prockop DJ. Marrow stromal cells as stem cells for continual renewal of nonhematopoietic tissues and as potential vectors for gene therapy. *J Cell Biochem* 1998;**72**:S284–5.
23. Dezawa M, Ishikawa H, Itokazu Y, Yoshihara T, Hoshino M, Takeda S, et al. Bone marrow stromal cells generate muscle cells and repair muscle degeneration. *Science* 2005;**309**:314–7.
24. Pittenger MF, Mackay AM, Beck SC, Jaiswal RK, Douglas R, Mosca JD, et al. Multilineage potential of adult human mesenchymal stem cells. *Science* 1999;**284**:143–7.
25. Squillaro T, Peluso G, Galderisi U. Clinical trials with mesenchymal stem cells: an update. *Cell Transplant* 2016;**25**:829–48.
26. Giordano A, Galderisi U, Marino IR. From the laboratory bench to the patients bedside: an update on clinical trials with mesenchymal stem cells. *J Cell Physiol* 2007;**211**:27–35.
27. Bartolucci J, Verdugo FJ, Larrea R, Abarzua E, Goset C, Rojo P, et al. Phase 1/2 randomized clinical trial of intravenous infusion of umbilical cord mesenchymal stem cells in patients with chronic cardiopathy with stable heart failure (RIMECARD). *Eur Heart J* 2016;**37**:527.
28. Zhu HB, Cao BR, Zhen ZP, Laxmi AA, Li D, Liu SR, et al. Controlled growth and differentiation of MSCs on grooved films assembled from monodisperse biological nanofibers with genetically tunable surface chemistries. *Biomaterials* 2011;**32**:4744–52.
29. Sonabend AM, Ulasov IV, Tyler MA, Rivera AA, Mathis JM, Lesniak MS. Mesenchymal stem cells effectively deliver an oncolytic adenovirus to intracranial glioma. *Stem Cells* 2008;**26**:831–41.
30. Kidd S, Spaeth E, Dembinski JL, Dietrich M, Watson K, Klopp A, et al. Direct evidence of mesenchymal stem cell tropism for tumor and wounding microenvironments using *in vivo* bioluminescent imaging. *Stem Cells* 2009;**27**:2614–23.
31. Dwyer RM, Potter-Beirne SM, Harrington KA, Lowery AJ, Hennessy E, Murphy JM, et al. Monocyte chemotactic protein-1 secreted by primary breast tumors stimulates migration of mesenchymal stem cells. *Clin Cancer Res* 2007;**13**:5020–7.
32. Jang SC, Kim OY, Yoon CM, Choi DS, Roh TY, Park J, et al. Bioinspired exosome-mimetic nanovesicles for targeted delivery of chemotherapeutics to malignant tumors. *ACS Nano* 2013;**7**:7698–710.
33. Rani S, Ryan AE, Griffin MD, Ritter T. Mesenchymal stem cell-derived extracellular vesicles: toward cell-free therapeutic applications. *Mol Ther* 2015;**23**:812–23.